Check for updates

Photonic Rashba effect from quantum emitters mediated by a Berry-phase defective photonic crystal

Kexiu Rong [1,3], Bo Wang [1,3], Avi Reuven[1], Elhanan Maguid [1], Bar Cohn[1], Vladimir Kleiner[1], Shaul Katznelson[2], Elad Koren[2] and Erez Hasman [1 ✉]

Heterostructures combining a thin layer of quantum emitters and planar nanostructures enable custom-tailored photoluminescence in an integrated fashion. Here, we demonstrate a photonic Rashba effect from valley excitons in a WSe$_2$ monolayer, which is incorporated into a photonic crystal slab with geometric phase defects, that is, into a Berry-phase defective photonic crystal. This phenomenon of spin-split dispersion in momentum space arises from a coherent geometric phase pickup assisted by the Berry-phase defect mode. The valley excitons effectively interact with the defects for site-controlled excitation, photoluminescence enhancement and spin-dependent manipulation. Specifically, the spin-dependent branches of photoluminescence in momentum space originate from valley excitons with opposite helicities and evidence the valley separation at room temperature. To further demonstrate the versatility of the Berry-phase defective photonic crystals, we use this concept to separate opposite spin states of quantum dot emission. This spin-enabled manipulation of quantum emitters may enable highly efficient metasurfaces for customized planar sources with spin-polarized directional emission.

Dipoles are ubiquitous in every branch of nanophotonics. Many quantum emitters, such as atoms, molecules, quantum dots (QDs) and transition metal dichalcogenide (TMD) monolayers, behave as dipoles in terms of emission characteristics[1,2]. Despite the inherently coherent emission from a single quantum emitter, the light from many independent quantum emitters, such as photoluminescence (PL), is generally incoherent and unpolarized, ascribed to the random locations, orientations and initial phases of the equivalent dipoles. Incorporation of quantum emitters and a nanophotonic system makes it possible to tailor the spatial and temporal profiles of the PL. The use of resonant nanostructures can enhance the emission intensities by the Purcell effect[3] and shape the emission spectra by wavelength selection[4]. Furthermore, a single nanoantenna or periodic nanostructures can increase the emission directionality and degree of polarization[5–7].

Recently, there has been a surge of interest in selectively manipulating the quantum emitters, that is, the valley excitons, in TMD monolayers[1,8,9], due to their potential as an alternative information carrier in valleytronics. The TMD monolayer possesses an inversion-asymmetric hexagonal crystal structure, which leads to opposite spins for electrons at the $\pm$K valleys; here, $\pm$K denote corners of the Brillouin zone of the electronic band structure, in which the energy–momentum extrema are referred to as valleys. Consequently, valley excitons can be selectively addressed and detected by the spin angular momentum of light according to the valley-dependent optical selection rule. Nevertheless, the short valley depolarization time prevents direct information transportation via valley excitons at room temperature, and an urge for a valley–photon interface emerges[8]. In particular, valley-selective directional emission remains a prerequisite for the spatial separation of the valley degree of freedom. Previous optical strategies for valley

separation were achieved by metallic nanostructures supporting plasmonic modes[8,9]. These structures inherit relatively high losses and incompatibility with the semiconductor technology. Besides, their limited functionalities hinder the pursuit of further valley processing that is demanded by valleytronics.

Two-dimensional arrays of customized nanoantennas, namely, metasurfaces, enable arbitrary control over the amplitude, phase and polarization states of light at the subwavelength scale[10–12]. The notable achievements of metasurfaces include spatially and spectrally interleaved multifunctionalities[13], spatiotemporal modulations[14,15], quantum entanglement[16] and others[17,18]. Particularly, geometric phase metasurfaces (GPMs), constructed of anisotropic nanoantennas with space-variant orientations, allow the manipulation of light by the spin degree of freedom[19]. This is enabled by the polarization evolution of light on the Poincaré sphere, which generates the spin-dependent Pancharatnam–Berry phase (geometric phase) for the spin-flipped components[10,20]. Hence, the GPMs represent an attractive candidate to perform the desired valley separation for TMD monolayers, inspired by spin-dependent photonic phenomena such as the spin Hall effect[21,22] and Rashba effect[23,24]. The photonic Rashba effect is manifested as a spin-split dispersion in momentum space, resembling a condensed-matter Rashba phenomenon in which the electrons' spin-degenerate bands split into dispersive branches with opposite spin-polarized states[25,26]. However, conventional GPMs are generally designed to operate under free-space plane waves. Therefore, they prevent an efficient interaction between nanoantennas and integrated quantum emitters. The emission then substantially leaks into free space without geometric phase pickup.

Here, we demonstrate a photonic Rashba effect from valley excitons in a WSe$_2$ monolayer using the Berry-phase defective photonic

[1]Micro and Nanooptics Laboratory, Faculty of Mechanical Engineering and Russell Berrie Nanotechnology Institute, Technion—Israel Institute of Technology, Haifa, Israel. [2]Faculty of Materials Science and Engineering, Technion—Israel Institute of Technology, Haifa, Israel. [3]These authors contributed equally: Kexiu Rong, Bo Wang. ✉e-mail: mehasman@technion.ac.il
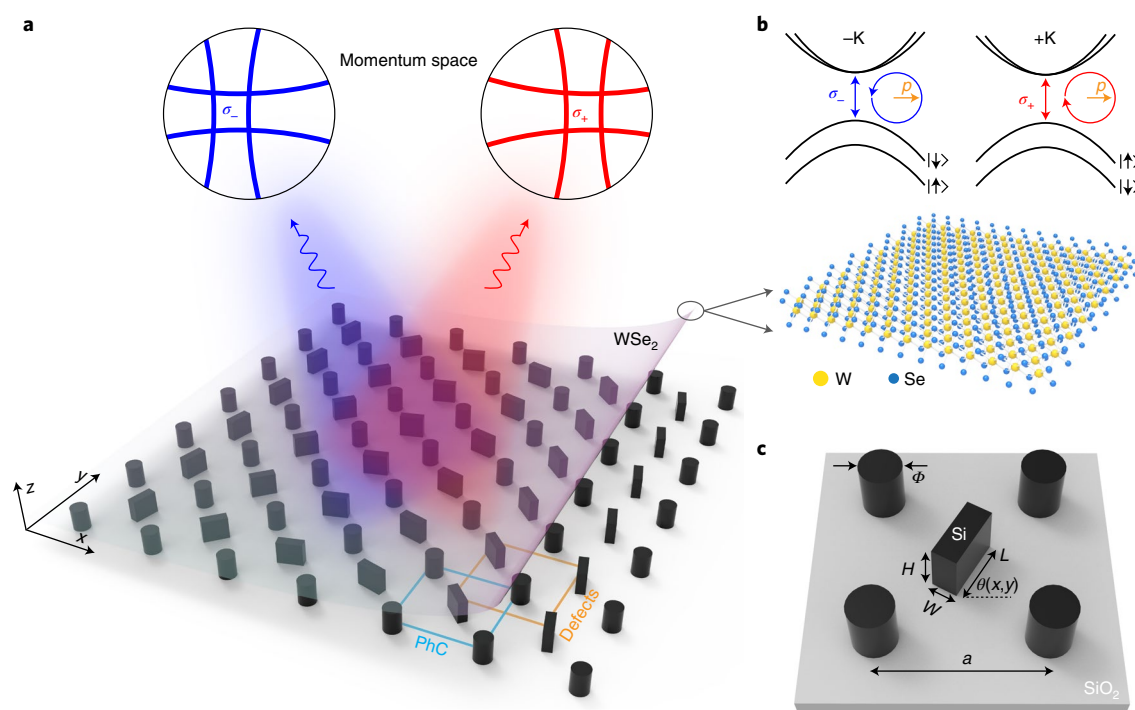
Fig. 1 | Illustration of photonic Rashba effect from quantum emitters mediated by a Berry-phase defective photonic crystal. a, Schematic of the Berry-phase defective PhC covered with a WSe$_2$ monolayer (only part of the structure is shown). The PhC slab is composed of isotropic nanopillars arranged in one lattice (highlighted by the cyan square), while the GPM is composed of anisotropic rectangular nanoantennas arranged in another lattice (highlighted by the orange square), serving as defects to the PhC slab. By virtue of the Berry-phase defect mode, the site-controlled excitation of valley excitons and space-variant polarization manipulation of the scattered PL are achieved at the defects, which give rise to a spin-split dispersion in momentum space, that is, a photonic Rashba effect, from valley excitons. **b**, Schematics of electronic band structures and valley-dependent optical selection rule for the $\pm K$ valley excitons. Due to the angular momentum conservation, the $-K$ ($+K$) valley exciton can be described as an in-plane left-handed (right-handed) circularly polarized dipole emitter with dipole moment $\mathbf{p}^\pm = p(\hat{\mathbf{x}} \pm i\hat{\mathbf{y}})$, which preferentially radiates to the spin-down σ_- (spin-up σ_+) branches in momentum space. The lower part shows the cartoon of the atomic structure for the WSe$_2$ monolayer. **c**, Structural details for one unit cell of the PhC slab embedding with an anisotropic nanoantenna. The heights for all the polycrystalline silicon nanostructures are $H = 300$ nm. The diameters of the nanopillars are $\Phi = 190$ nm, and the lattice constant of the square lattice is $a = 440$ nm. The rectangular nanoantennas have an in-plane dimension of $L = 170$ nm and $W = 70$ nm, and they are imparted with an orientation angle profile $\theta(x,y) = \pi x/Na$, where N ($N = 6$) is the number of lattice periods for π rotation of the nanoantennas in the x direction.

crystal (PhC), which is constructed by embedding a GPM into a PhC slab as defects (Fig. 1a). The PhC slab is a planar structure that combines two-dimensional periodicity and index guiding in the third dimension[27], creating a range of frequencies (band gap) for which light is forbidden to exist. By virtue of this band gap, the insertion of the GPM into the PhC slab gives rise to a near-field Berry-phase defect mode, which couples the defects for an effective interaction with the integrated quantum emitters. This leads to coherent geometric phase accumulations for individual quantum emitters as the defect mode recouples to free space. Consequently, a spin-split dispersion from valley excitons is observed in momentum space, manifesting as the photonic Rashba effect. Particularly, the spin-up and spin-down branches correspond to emission from the $+K$ and $-K$ valley excitons (Fig. 1b), respectively, indicating the valley separation in momentum space at room temperature.

Principle of Berry-phase defective PhC

The Berry-phase defective PhC is composed of a PhC slab with isotropic nanopillars and a GPM with space-variant anisotropic nanoantennas that serve as defects (Fig. 1a,c). Specifically, the band gap of the PhC slab (grey area in Fig. 2a) is designed to cover the PL wavelengths of the WSe$_2$ monolayer (Fig. 2c). The GPM, assigned with a space-variant orientation angle profile $\theta(x,y) = \pi x/Na$, provides

a route to achieve space-variant polarization manipulation of the scattered light; here, N ($N = 6$) is the number of lattice periods (a) for π rotation of the anisotropic nanoantennas in the x direction. Due to the insertion of the GPM into the PhC slab, a defect band residing in the band gap emerges (green dots in Fig. 2a). This defect band can be described by the dispersion relation derived from the classical wave analogue of the tight-binding model[28–30], as shown by the solid curves in Fig. 2b. This property reveals a hopping mechanism between neighbouring defects, which leads to a coupled defect mode due to the superposition of individual localized defect modes (see the section on simulation in the Methods). The calculated field distribution for the coupled defect mode at the M point of the defect band is depicted by the two right panels in Fig. 2d, where two differently oriented nanoantennas are shown (see Supplementary Fig. 3b for the field distribution in a complete unit cell). For comparison, the field distributions for the isolated nanoantenna and PhC slab are also displayed in Fig. 2d. The resonance intensity of the isolated nanoantenna is enhanced by an order of magnitude when embedded in the PhC slab (Fig. 2e). This leads to an emission rate enhancement of quantum emitters by the Purcell effect, which, in combination with the defect-enhanced excitation efficiency, results in the site-controlled excitation and PL enhancement of the quantum emitters around the defects (Supplementary Fig. 5). Hence, the Berry-phase defective PhC provides a natural way to
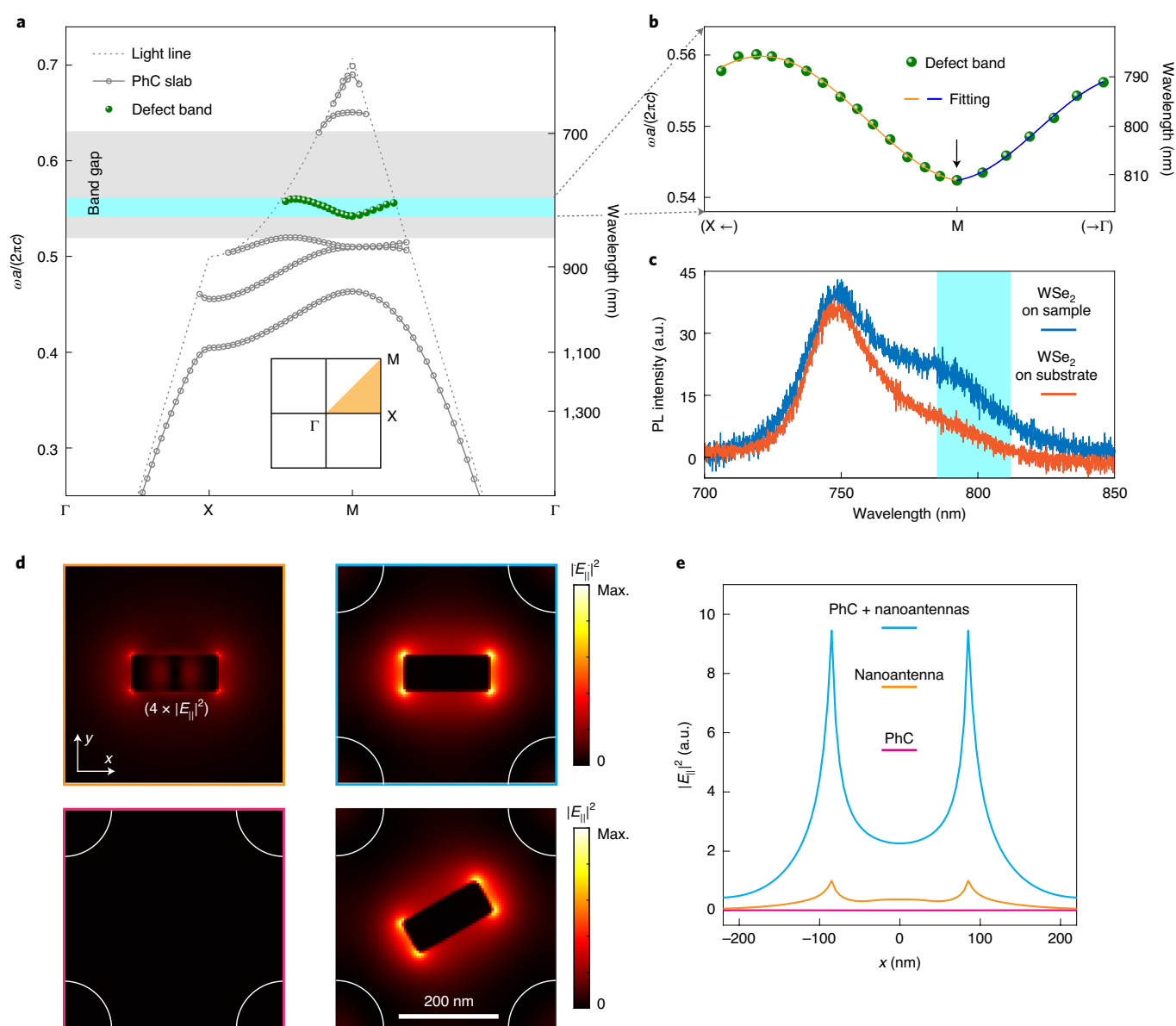
Fig. 2 | Principle of Berry-phase defective PhC. a, Calculated defect band (green dots) for Berry-phase defective PhC. The grey circles denote the band structure for the square PhC slab without defects, in which the grey area indicates the band gap. Here, ω is the angular frequency and c is the speed of light in free space. Inset, first Brillouin zone of the square lattice labelled with high symmetry points. **b**, Zoomed-in defect band fitted by the dispersion relation derived from the classical wave analogue of the tight-binding model. The fittings are separately implemented along the M–X and M–Γ directions with appropriate coupling factors and distances between neighbouring defects. More details can be found in the section on simulation in the Methods and in the Supplementary text section 3. **c**, Measured PL spectra of the WSe$_2$ monolayer on Berry-phase defective PhC (Fig. 3c) and substrate. The wavelength range of the cyan area equals that of the defect band shown in **a**. **d**, Intensity distributions of in-plane electric field ($E_{\parallel}$) for the isolated nanoantenna (top-left panel), PhC slab (bottom-left panel) and Berry-phase defective PhC (two right panels). Two defects of the Berry-phase defective PhC along $\theta = 0$ (top-right panel) and $\pi/6$ (bottom-right panel) are shown. The simulation wavelength corresponds to the M point of the defect band, as indicated by a black arrow in **b**. These distributions are extracted across the plane of $z = 60$ nm, with the midplane of the nanostructures located at $z = 0$. Only one unit cell of the PhC slab is displayed for the last three cases, in which the white quarter circles indicate the contours of nanopillars. Max., maximum. **e**, Extracted intensity profiles along the x direction. These profiles (cyan, orange and magenta curves) are extracted across the upper edge of the nanoantenna from the intensity distributions (cyan, orange and magenta boundaries) shown in **d**. The intensity profile of the isolated nanoantenna is used for normalization.

achieve site-controlled quantum emitters for tailored light–matter interaction, which circumvents the complex and challenging procedures to selectively place the quantum emitters at the defects.

Moreover, the local field distributions of the coupled defect mode undergo a space-variant rotation following the orientations of the defects (Fig. 2d). This enables a space-variant polarization

manipulation of the scattered light from the defects, resulting in the spin-dependent geometric phase pickup. Accordingly, the coupled defect mode is referred to as the Berry-phase defect mode, whereby the quantum emitters can effectively interact with the defects in a sufficiently long range, in contrast to the case without the PhC slab (Supplementary Fig. 4). Consequently, we expect to observe a
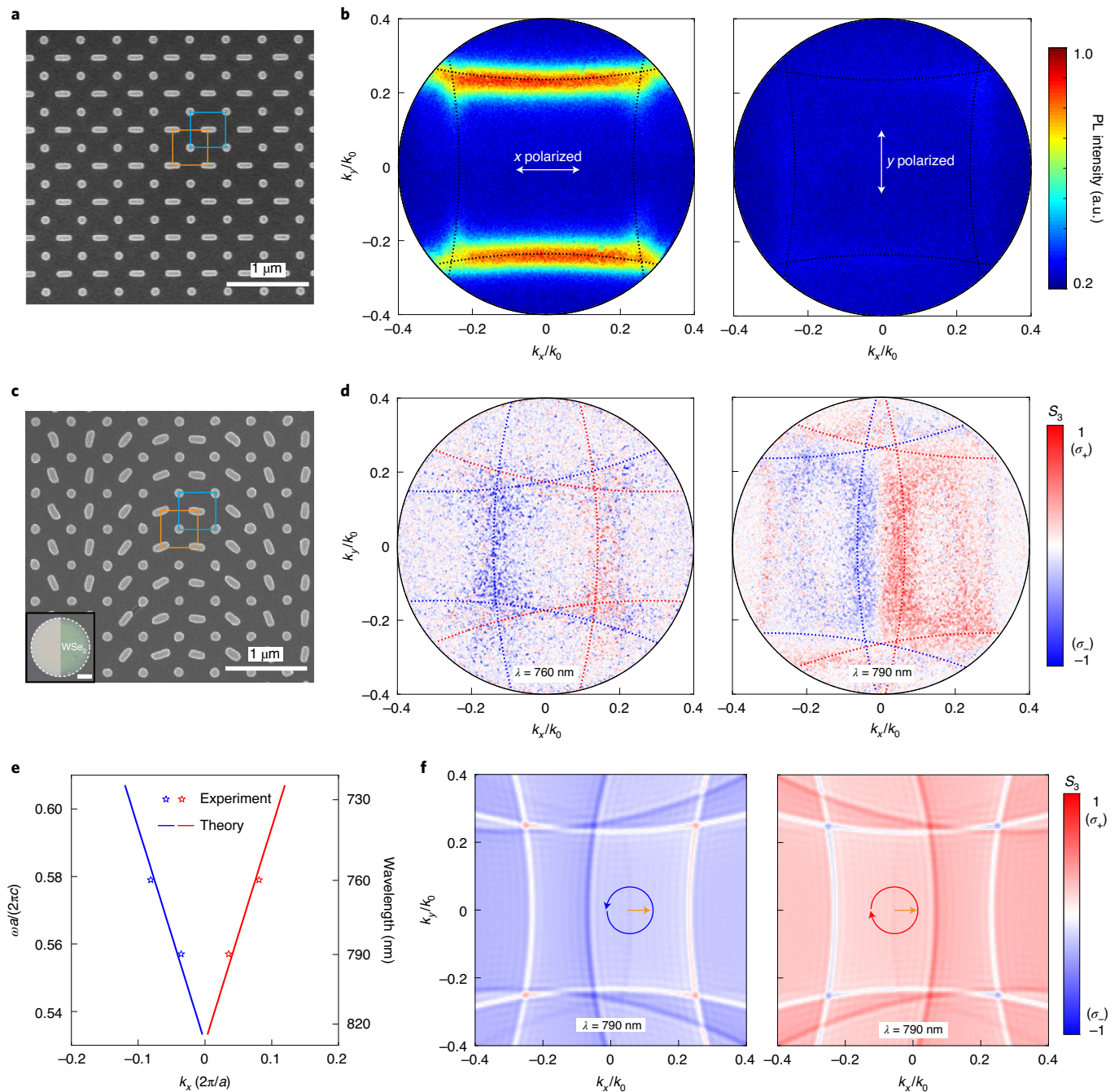
Fig. 3 | Observation of photonic Rashba effect from valley excitons in a WSe$_2$ monolayer. a, SEM image of a defective PhC with all the defects possessing the same orientation, $\theta(x,y) = 0$. The PhC slab and defect lattice are highlighted by cyan and orange squares, respectively. **b**, Measured x- and y-polarized PL intensity distributions in momentum space. A bandpass filter is used to filter out the PL at the central wavelength of 790 nm with a half-maximum bandwidth of 10 nm. The circular boundary corresponds to the numerical aperture (NA = 0.4) of the collection objective. The dotted black curves denote calculations based on the standard momentum-matching condition. The k_0 denotes the free-space wavenumber. **c**, SEM image of a Berry-phase defective PhC. Inset, optical microscope images of the Berry-phase defective PhC before (left part) and after (right part) the WSe$_2$ monolayer coverage (scale bar, 50 μm). For comparison, only half of the structure is displayed for each case since the whole structure is covered by the monolayer. **d**, Measured spin-split modes in momentum space at two wavelengths: 760 nm and 790 nm. The dotted red (σ_+) and blue (σ_-) curves denote calculations based on the spin–orbit momentum-matching condition. **e**, Extracted spin-split dispersion along $k_y = 0$. The stars denote experimental results extracted from **d**, while the solid curves denote the theoretical spin-split dispersion from the spin–orbit momentum-matching condition. **f**, Calculated valley separation in momentum space. The left and right panels correspond to calculations using left- and right-handed circularly polarized dipole emitters, respectively. For each case, six in-plane circular dipole emitters, located at the defect locations in one unit cell, are considered.

directional emission from the incorporated quantum emitters, due to the large spatial coherence length of the near-field Berry-phase defect mode.

Photonic Rashba effect from valley excitons

To experimentally demonstrate the photonic Rashba effect, the Berry-phase defective PhC was fabricated on a polycrystalline silicon

film using electron-beam lithography techniques and covered with a highly crystalline WSe$_2$ monolayer (see the section on fabrication in the Methods). The monolayer character was verified by Raman spectra, shown in Supplementary Fig. 6. The diameter of the fabricated Berry-phase defective PhC is $D_1 = 200\,\mu m$ (indicated by a dashed circle in the inset of Fig. 3c), and a scanning electron microscopy (SEM) image showing details of the nanostructures is depicted in Fig. 3c. Excited by a continuous-wave laser with linear polarization (wavelength of $\lambda = 532\,nm$ and spot diameter of $D_2 = 100\,\mu m$), both the $+K$ and $-K$ valley excitons were populated in the WSe$_2$ monolayer at room temperature[9] (see the section on measurement in the Methods). The $\pm K$ valley excitons radiated as in-plane circularly polarized dipoles with opposite helicities[1], which interacted with the planar nanostructures by coupling to the near-field Berry-phase defect mode, and subsequently scattered to free space for measurements. The measured emission spectrum of the WSe$_2$ monolayer on the Berry-phase defective PhC is depicted in Fig. 2c, where an enhancement (compared to the case on the substrate) is observed at the long-wavelength tail of the PL, in agreement with the calculated wavelength range for the defect band (cyan area in Fig. 2c). In addition, we experimentally verified the strong polarization manipulation enabled by the Berry-phase defective PhC. This is achieved by fabricating a defective PhC with all the defects possessing the same orientation $\theta(x,y) = 0$ (Fig. 3a). The measured PL from the covered WSe$_2$ monolayer in momentum space is strongly polarized along the orientation of the defects, that is, x polarization (Fig. 3b), validating the polarization manipulation from the defects.

Hence, spin-dependent geometric phases arise from the Berry-phase defective PhC since the polarization state of the scattered PL rotates with the space-variant defects. Consequently, the spin-split modes were measured in momentum space around the wavelength of $\lambda = 790\,nm$ (Fig. 3d and Supplementary Fig. 7), consistent with the measured wavelength range for PL enhancement (Fig. 2c). These spin-resolved momentum spaces were obtained by measuring the S_3 component of the Stokes vector. This component, defined as $S_3(\mathbf{k}_{||}) = [I_{\sigma+}(\mathbf{k}_{||}) - I_{\sigma-}(\mathbf{k}_{||})]/[I_{\sigma+}(\mathbf{k}_{||}) + I_{\sigma-}(\mathbf{k}_{||})]$, describes the portion of circular polarization for the scattered PL. Here, $\mathbf{k}_{||} = k_x\hat{\mathbf{x}} + k_y\hat{\mathbf{y}}$ ($\hat{\mathbf{x}}$ and $\hat{\mathbf{y}}$ are unit vectors) is the in-plane wave vector in momentum space; $I_{\sigma+}$ and $I_{\sigma-}$ are PL intensities for opposite spin states discriminated by a circular polarization analyser. Theoretically, we find that these spin-split modes obey the spin–orbit momentum-matching condition $\mathbf{k}_{||}^{g,h} = n_{eff}\mathbf{k}_0 + g\mathbf{G}_1 + h\mathbf{G}_2 + \sigma\mathbf{k}_s$ (ref. [24]), as indicated by the dotted red ($\sigma = 1$) and blue ($\sigma = -1$) curves in Fig. 3d. Here, $n_{eff}\mathbf{k}_0$ is the effective in-plane wave vector for the Berry-phase defect mode, $\mathbf{G}_1$ and $\mathbf{G}_2$ are basic reciprocal lattice vectors of the GPM and g and h ($g, h \in \{0, 1, -1\}$) are indices of the radiative mode with the in-plane wave vector $\mathbf{k}_{||}^{g,h}$. The spin-dependent term $\sigma\mathbf{k}_s$, which equals $[-2\sigma\partial\theta(x,y)/\partial x]\hat{\mathbf{x}}$, arises from the gradient of geometric phase pickup $\phi_g = -2\sigma\theta(x,y)$ due to the space-variant polarization manipulation. Moreover, the extracted spin-split dispersion, such as that along $k_y = 0$ (Fig. 3e), supports the claim of a photonic Rashba effect from valley excitons in the WSe$_2$ monolayer. The measured spatial coherence length of the PL is $l_c = 2\pi/\Delta k \approx 17\lambda$ ($\lambda = 790\,nm$), which indicates a sufficiently long coherent interaction distance for the valley excitons and defect nanoantennas; here, Δk denotes the half-maximum width of the measured mode in momentum space.

The observed photonic Rashba effect can be explained via an effective interaction between in-plane circularly polarized dipole emitters (equivalence of valley excitons) and the defect lattice, that is enabled by the Berry-phase defect mode. Considering the site-controlled excitation of valley excitons around the defects, we assume a two-dimensional array of dipoles $\mathbf{p}_n$ located above defects with locations and orientations $(\mathbf{r}_n, \theta_n)$, where n is an integer labelling the dipoles and defects. The defects are treated as space-variant polarizers with transmission axes along $\hat{\mathbf{P}}_n = \cos\theta_n\hat{\mathbf{x}} + \sin\theta_n\hat{\mathbf{y}}$, as

validated by the measured polarization locking along the defects (Fig. 3b). For a single dipole emitter $\mathbf{p}_m$, its radiated electric field at the n-th defect is $\mathbf{E}^m(\mathbf{r}_n)$, which is calculated by the Green function (see the section on theory in the Methods). The resultant electric field in momentum space $\mathbf{U}^m(\mathbf{k}_{||})$ is determined by the coherent addition of the scattered light from all the defects; that is,

$$\mathbf{U}^m(\mathbf{k}_{||}) = \mathcal{F}\left\{\sum_n \left[\mathbf{E}^m(\mathbf{r}_n) \cdot \hat{\mathbf{P}}_n\right]\hat{\mathbf{P}}_n\right\}, \quad (1)$$

where $\mathcal{F}\{\}$ refers to the Fourier transform. Consequently, geometric phases emerge for a single dipole emitter ascribed to the space-variant polarization manipulation embedded within $\hat{\mathbf{P}}_n$ in equation (1). Specifically, for the circular dipole of either left (+) or right (−) handedness with dipole moment $\mathbf{p}_m^{\pm} = p(\hat{\mathbf{x}} \pm i\hat{\mathbf{y}})$ $(i = \sqrt{-1})$, the emerging geometric phase for its spin-flipped component of radiation is $\phi_g(\mathbf{r}_n) = \arg\left\{\left[(\mathbf{E}_{\pm}^m(\mathbf{r}_n) \cdot \hat{\mathbf{P}}_n)\hat{\mathbf{P}}_n\right] \cdot \hat{\sigma}^{\mp}\right\} - \phi_d(\mathbf{r}_n)$. Here, $\mathbf{E}_{\pm}^m(\mathbf{r}_n)$ is the radiated electric field for the left- or right-handed circular dipole; $\hat{\sigma}^{\mp} = (\hat{\mathbf{x}} \mp i\hat{\mathbf{y}})/\sqrt{2}$ is a unit operator that projects the radiation to the spin-flipped state; and $\phi_d(\mathbf{r}_n)$ denotes a dynamic phase due to the phase accumulation from the source $\mathbf{p}_m$ to the n-th defect, and it equals the phase for the spin-maintained component of radiation, that is, $\phi_d(\mathbf{r}_n) = \arg\left\{\left[(\mathbf{E}_{\pm}^m(\mathbf{r}_n) \cdot \hat{\mathbf{P}}_n)\hat{\mathbf{P}}_n\right] \cdot \hat{\sigma}^{\pm}\right\}$. Based on this principle, we revealed that $\phi_g(\mathbf{r}_n) = -2\sigma\theta_n$ (see the Supplementary text section 6), in agreement with the spin-dependent term $\sigma\mathbf{k}_s$ in the spin–orbit momentum-matching condition. Equation (1) leads to a well-defined spin distribution in momentum space that can be calculated by $S_3^m = -2\mathrm{Im}(U_x^m U_y^{m*})/(|U_x^m|^2 + |U_y^m|^2)$; here, Im () refers to the calculation of the imaginary part and the asterisk denotes the complex conjugate. For multiple independent dipole emitters, the spin-resolved momentum space equals the incoherent addition of individual spin distributions[31], that is, $\bar{S}_3 = -2\sum_m \mathrm{Im}(U_x^m U_y^{m*})/\sum_m (|U_x^m|^2 + |U_y^m|^2)$. For the Berry-phase defective PhC shown in Fig. 3c, the calculated $\bar{S}_3(\mathbf{k}_{||})$ for multiple left-handed circularly polarized dipole emitters (equivalence of the $-K$ valley excitons) is depicted by the left panel of Fig. 3f, where the spin modes match the measured spin-down branches (blue curves in the right panel of Fig. 3d). Similarly, good agreement is also observed between the measured spin-up branches and those calculated from multiple right-handed circularly polarized dipole emitters (equivalence of the $+K$ valley excitons). Hence, the emissions from valley excitons with opposite helicities are separated in momentum space, manifesting as the photonic Rashba effect.

Photonic Rashba effect from QDs

The Berry-phase defective PhCs are underpinned by a basic interaction between circular dipole emitters with opposite helicities and nanostructures, which is applicable to other quantum emitters beyond valley excitons. Due to the strong spatial confinement, excitons can also be excited in QDs at room temperature[32]. By incorporating QDs into the Berry-phase defective PhC, these site-controlled excitons radiate as linearly polarized dipoles oriented along the defects, and each of these dipoles is equal to the superposition of two opposite-handed circularly polarized ones. For demonstration, we fabricated the Berry-phase defective PhC that was covered by a thin hydrogen silsesquioxane (HSQ) layer ($t = 70\,nm$) doped with randomly placed QDs (Fig. 4a). Similar spin separations as those for the WSe$_2$ monolayer are also observed (Fig. 4b and Supplementary Figs. 10 and 11), with the difference that the emission from each exciton splits to spin-up and spin-down branches simultaneously. The concept of Berry-phase defective PhCs can be implemented in different PhC structures that support photonic band gaps, such as the Kagome one. The Kagome lattice is a depleted version of the
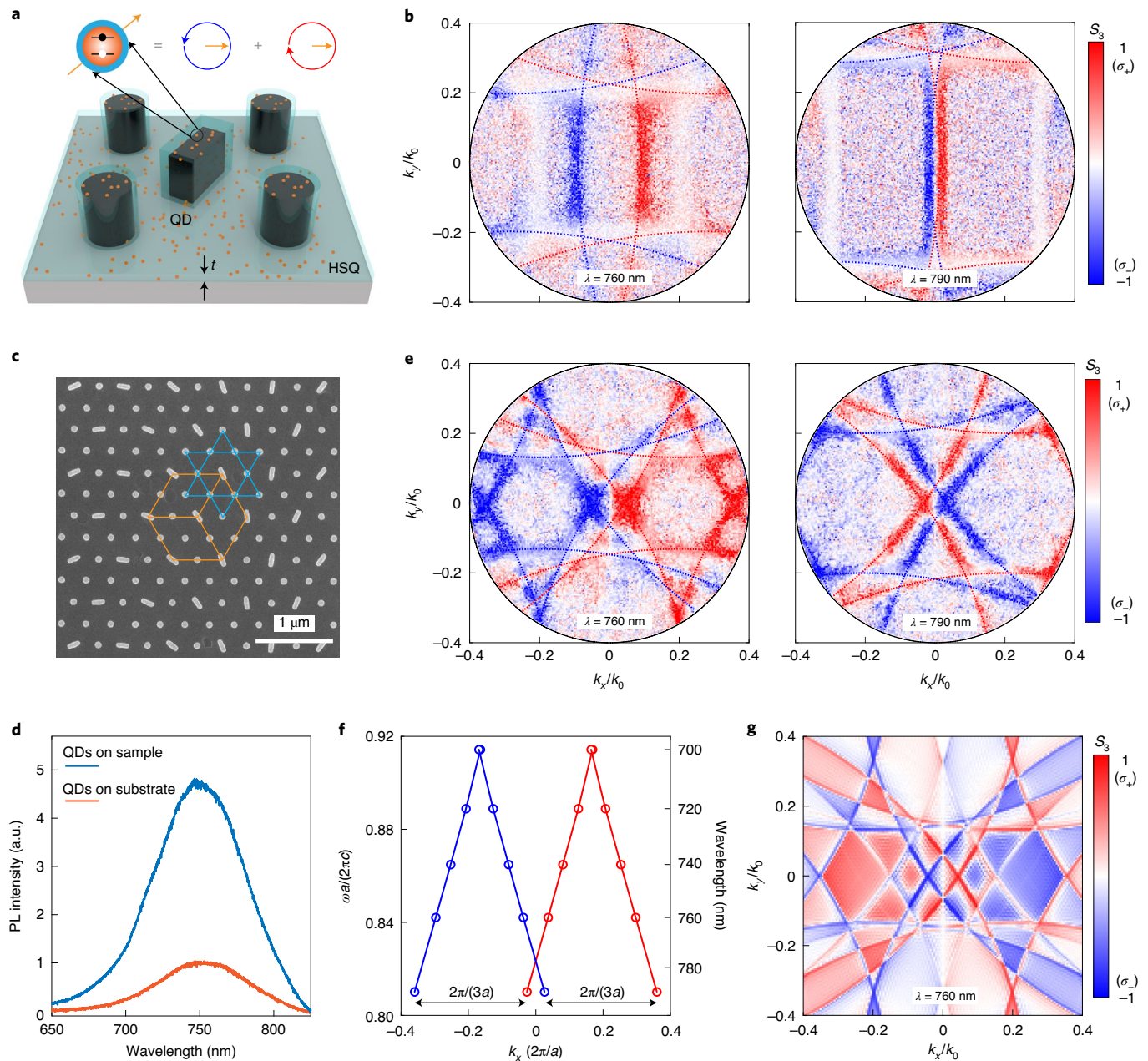
Fig. 4 | Observation of photonic Rashba effect from QDs. a, Schematic of the Berry-phase defective PhC incorporated with QDs. These site-controlled QDs, doped in a thin HSQ layer ($t = 70$ nm), radiate as linearly polarized dipoles oriented along the defects, and each of these dipoles equals the superposition of two opposite-handed circularly polarized ones. **b,** Measured spin-split modes in momentum space. The dotted red (σ_+) and blue (σ_-) curves denote calculations based on the spin–orbit momentum-matching condition. **c,** SEM image of a Kagome–hexagonal Berry-phase defective PhC. The PhC slab and defect lattice are highlighted by a cyan hexagram and orange hexagon, respectively. The lattice constants for Kagome and hexagonal lattices are $a = 320$ nm and 640 nm, respectively. **d,** Measured PL enhancement for the Kagome–hexagonal Berry-phase defective PhC (blue curve), as compared to the case of a bare QD-doped HSQ film (orange curve). **e,** Measured spin-split modes in momentum space for the Kagome–hexagonal Berry-phase defective PhC. The measured spatial coherence length for the PL is $l_c \approx 22\lambda$ ($\lambda = 790$ nm). **f,** Extracted spin-split dispersion along $k_y = 0$ for the Kagome–hexagonal Berry-phase defective PhC. **g,** Calculated spin-resolved momentum space for the Kagome–hexagonal Berry-phase defective PhC. Twelve linearly polarized dipole emitters, sharing the same positions and orientations as the defects in one unit cell, are considered.

triangular lattice that favours the formation of a band gap[33], and its sparsely arranged photonic atoms also enable the insertion of defect nanoantennas as a hexagonal lattice (see Fig. 4c for the SEM image of the Kagome–hexagonal Berry-phase defective PhC). Simulations of the defect band in this case can be found in the Supplementary text section 9, and the measured PL enhancement is depicted in Fig. 4d. Moreover, the observed spin-split modes inherit the symmetry

of the hexagonal lattice (Fig. 4e and Supplementary Fig. 15), and the extracted spin-split dispersion also shows the photonic Rashba effect (Rashba split of $2\pi/3a$). Theoretically, these spin-split modes can be interpreted by assuming linearly polarized dipole emitters in equation (1), and the calculated spin-resolved momentum space is depicted in Fig. 4g, in agreement with the measurement (left panel of Fig. 4e). As a comparison, we also fabricated the GPM without

the PhC slab, where a chiral mode rather than the photonic Rashba effect is observed from the incorporated QDs, due to the negligible geometric phase pickup from the nanoantennas (Supplementary text section 11).

Conclusions

We have demonstrated the photonic Rashba effect from valley excitons in a WSe$_2$ monolayer, which is incorporated in the Berry-phase defective PhC. This geometric-phase-induced valley separation establishes a multifunctional interface between valleytronics and photonics via all-silicon nanostructures, which may facilitate viable applications of valleytronics in semiconductor platforms. Moreover, the revealed phase and polarization locking from Berry-phase defects can also be implemented to observe the spin-split emission from linear dipole sources, such as excitons in QDs. These polarization-locked linear dipoles in the near field can be considered as a superposition of two orthogonal circular ones. Based on this mechanism, we have also demonstrated a separation of emission with opposite spin states for QDs. Incorporating the approach of Berry-phase defects with a high-quality-factor PhC cavity can achieve the coherent addition of multiple dipole sources; this will result in a collapse of the continuous spin-split branches into discrete points (see Supplementary Fig. 9). Although we demonstrate the photonic Rashba effect only from PL of the described quantum emitters, the same effect should hold equally well for electroluminescence or chemiluminescence to observe spin-polarized directional emission. We envision our Berry-phase defective PhCs as a versatile platform for integrated spin manipulation, which may inspire further investigations in heterostructures containing a quantum emitter and metasurface. The foreseen applications include wavefront manipulation of single quantum emitters and spin engineering in nanostructured light-emitting diodes.

Online content

Any methods, additional references, Nature Research reporting summaries, source data, extended data, supplementary information, acknowledgements, peer review information; details of author contributions and competing interests; and statements of data and code availability are available at https://doi.org/10.1038/s41565-020-0758-6.

References

1. Schuller, J. A. et al. Orientation of luminescent excitons in layered nanomaterials. *Nat. Nanotechnol.* **8**, 271–276 (2013).
2. Empedocles, S. A., Neuhauser, R. & Bawendi, M. G. Three-dimensional orientation measurements of symmetric single chromophores using polarization microscopy. *Nature* **399**, 126–130 (1999).
3. Englund, D. et al. Controlling the spontaneous emission rate of single quantum dots in a two-dimensional photonic crystal. *Phys. Rev. Lett.* **95**, 013904 (2005).
4. Staude, I., Pertsch, T. & Kivshar, Y. S. All-dielectric resonant meta-optics lightens up. *ACS Photonics* **6**, 802–814 (2019).
5. Cihan, A. F., Curto, A. G., Raza, S., Kik, P. G. & Brongersma, M. L. Silicon Mie resonators for highly directional light emission from monolayer MoS$_2$. *Nat. Photon.* **12**, 284–290 (2018).
6. de Leo, E. et al. Polarization multiplexing of fluorescent emission using multiresonant plasmonic antennas. *ACS Nano* **11**, 12167–12173 (2017).
7. Curto, A. G. et al. Unidirectional emission of a quantum dot coupled to a nanoantenna. *Science* **329**, 930–933 (2010).
8. Gong, S.-H., Alpeggiani, F., Sciacca, B., Garnett, E. C. & Kuipers, L. Nanoscale chiral valley-photon interface through optical spin-orbit coupling. *Science* **359**, 443–447 (2018).
9. Sun, L. et al. Separation of valley excitons in a MoS$_2$ monolayer using a subwavelength asymmetric groove array. *Nat. Photon.* **13**, 180–184 (2019).
10. Bomzon, Z., Biener, G., Kleiner, V. & Hasman, E. Space-variant Pancharatnam-Berry phase optical elements with computer-generated subwavelength gratings. *Opt. Lett.* **27**, 1141–1143 (2002).
11. Yu, N. et al. Light propagation with phase discontinuities: generalized laws of reflection and refraction. *Science* **334**, 333–337 (2011).
12. Kildishev, A. V., Boltasseva, A. & Shalaev, V. M. Planar photonics with metasurfaces. *Science* **339**, 1232009 (2013).
13. Maguid, E. et al. Photonic spin-controlled multifunctional shared-aperture antenna array. *Science* **352**, 1202–1206 (2016).
14. Wang, Q. et al. Optically reconfigurable metasurfaces and photonic devices based on phase change materials. *Nat. Photon.* **10**, 60–65 (2016).
15. Shaltout, A. M., Shalaev, V. M. & Brongersma, M. L. Spatiotemporal light control with active metasurfaces. *Science* **364**, eaat3100 (2019).
16. Stav, T. et al. Quantum entanglement of the spin and orbital angular momentum of photons using metamaterials. *Science* **361**, 1101–1104 (2018).
17. Pors, A., Albrektsen, O., Radko, I. P. & Bozhevolnyi, S. I. Gap plasmon-based metasurfaces for total control of reflected light. *Sci. Rep.* **3**, 2155 (2013).
18. Lin, D., Fan, P., Hasman, E. & Brongersma, M. L. Dielectric gradient metasurface optical elements. *Science* **345**, 298–302 (2014).
19. Bliokh, K. Y., Rodríguez-Fortuño, F. J., Nori, F. & Zayats, A. V. Spin-orbit interactions of light. *Nat. Photon.* **9**, 796–808 (2015).
20. Berry, M. V. Quantal phase factors accompanying adiabatic changes. *Proc. R. Soc. Lond. A* **392**, 45–57 (1984).
21. Wang, B., Rong, K., Maguid, E., Kleiner, V. & Hasman, E. Probing nanoscale fluctuation of ferromagnetic meta-atoms with a stochastic photonic spin Hall effect. *Nat. Nanotechnol.* **15**, 450–456 (2020).
22. Wang, B. et al. Photonic topological spin Hall effect mediated by vortex pairs. *Phys. Rev. Lett.* **123**, 266101 (2019).
23. Dahan, N., Gorodetski, Y., Frischwasser, K., Kleiner, V. & Hasman, E. Geometric Doppler effect: spin-split dispersion of thermal radiation. *Phys. Rev. Lett.* **105**, 136402 (2010).
24. Shitrit, N. et al. Spin-optical metamaterial route to spin-controlled photonics. *Science* **340**, 724–726 (2013).
25. Rashba, E. I. Properties of semiconductors with an extremum loop. 1. Cyclotron and combinational resonance in a magnetic field perpendicular to the plane of the loop. *Sov. Phys. Solid State* **2**, 1109–1122 (1960).
26. Ishizaka, K. et al. Giant Rashba-type spin splitting in bulk BiTeI. *Nat. Mater.* **10**, 521–526 (2011).
27. Johnson, S. G., Fan, S., Villeneuve, P. R., Joannopoulos, J. D. & Kolodziejski, L. A. Guided modes in photonic crystal slabs. *Phys. Rev. B* **60**, 5751–5758 (1999).
28. Yariv, A., Xu, Y., Lee, R. K. & Scherer, A. Coupled-resonator optical waveguide: a proposal and analysis. *Opt. Lett.* **24**, 711–713 (1999).
29. Bayindir, M., Temelkuran, B. & Ozbay, E. Tight-binding description of the coupled defect modes in three-dimensional photonic crystals. *Phys. Rev. Lett.* **84**, 2140–2143 (2000).
30. Richter, S. et al. Periodically arranged point defects in two-dimensional photonic crystals. *Phys. Rev. B* **70**, 193302 (2004).
31. Goldstein, D. H. & Collett, E. *Polarized Light* 2nd edn (Marcel Dekker, 2003).
32. Brus, L. E. Electron-electron and electron-hole interactions in small semiconductor crystallites: the size dependence of the lowest excited electronic state. *J. Chem. Phys.* **80**, 4403–4409 (1984).
33. Garcia-Adeva, A. Band gap atlas for photonic crystals having the symmetry of the kagomé and pyrochlore lattices. *New J. Phys.* **8**, 86 (2006).

Methods

Sample fabrication. The 300-nm-thick polycrystalline silicon (poly-Si) film was grown on a fused silica (SiO_2) substrate at a temperature of 590 °C. Subsequently, a 100-nm-thick HSQ film serving as the negative-tone electron-beam resist was spin-coated above the poly-Si film. After baking at 120 °C for 4 min, the HSQ film was patterned by electron-beam lithography (Raith EBPG system, 100 kV) and developed in the developer solution (MiF 726) for 70 s, resulting in the fabrication of the desired mask on the HSQ film. To transfer the mask pattern to the underlying poly-Si film, deep reactive-ion etching (F-ICP Plasma Therm system) was employed to etch the uncovered poly-Si film for 30 s. The HSQ mask was removed by reactive-ion etching (CHF_3 and O_2) for 6 min. Finally, a highly crystalline WSe_2 monolayer (1 cm × 1 cm; 2D Semiconductors) grown by chemical vapour deposition was transferred above the nanostructures. Alternatively, commercially available QDs (CdTe/CdSe/ZnS; Creative Diagnostics) were uniformly dispersed in the HSQ solution and spin-coated above the nanostructures, with a thickness of approximately 70 nm. The diameters of the near-infrared-emitting CdTe/CdSe/ZnS core/shell/shell QDs were approximately 6 nm. The measured quantum efficiencies for the as-grown WSe_2 monolayer and QDs were approximately 10% and 60%, respectively, which could be greatly boosted by the Purcell effect in Berry-phase defective PhCs. The schematic for the fabrication processes can be found in Supplementary Fig. 1.

Optical measurement and data analysis. All the optical measurements were conducted in ambient environment at room temperature. The linearly polarized pump beam ($\lambda = 532$ nm) from a continuous-wave laser first passed through a short-pass filter to eliminate any spectrum remaining at the PL wavelengths of the quantum emitters. The filtered pump beam was subsequently focused by a lens (focal length $f = 10$ cm) to excite the quantum emitters incorporated in the samples. The PL scattered from the nanostructures was collected by an objective (Mitutoyo M Plan NIR 20; NA, 0.4) and spectrally selected by different bandpass filters (see Supplementary Fig. 7a for transmission spectra), which simultaneously blocked the pump beam. To enable the spin projection of the collected PL in momentum space, the magnified PL image after the objective was Fourier transformed by a second lens ($f = 10$ cm). Here, a circular polarization analyser (a quarter-wave plate followed by a linear polarizer) was utilized to discriminate opposite spin states, which were imaged by an electron-multiplying charge-coupled device (Andor iXon). Alternatively, the collected PL was refocused by a lens ($f = 10$ cm) to a multimode fibre, which was connected to a spectrometer (Horiba iHR320) for spectrum analysis. It was experimentally verified that the polarization states (linear or circular polarization) of the pump beam and the orientations (nanostructures or substrate facing the objective) of the sample had negligible influence on the measured results. The schematic for the experimental set-up can be found in Supplementary Fig. 2.

The experimental signal-to-noise ratio could be enhanced by eliminating the homogenous background. There were two kinds of homogenous background that contributed to the captured images. One was from the dark counts of the charge-coupled device, and the other was from the PL without interaction with the planar nanostructures. We subtracted the homogenous background, leaving a background-free pattern that originated from the interaction between the PL and nanostructures. To avoid being divided by numbers near zero in the calculation of $S_3(\mathbf{k}_\parallel) = [I_{\sigma+}(\mathbf{k}_\parallel) - I_{\sigma-}(\mathbf{k}_\parallel)]/[I_{\sigma+}(\mathbf{k}_\parallel) + I_{\sigma-}(\mathbf{k}_\parallel)]$, a small offset was added to the denominator for areas with only background[9]. In the fitting of the measured modes in momentum space, we chose a suitable effective refractive index n_{eff} (1.3–1.5) for the coupled defect mode in the momentum-matching condition. To obtain the spin-split dispersion, we first extracted the PL intensity profile along $k_y = 0$ from the spin-projected measurement $I_{\sigma\pm}(\mathbf{k}_\parallel)$ under a specific wavelength, which was determined by the central wavelength of the bandpass filter. Following that extraction, each spin-dependent peak on the intensity profile was fitted by a Gaussian function, the centre of which was assigned as the wave vector of the corresponding spin mode. The same procedure was repeated for other wavelengths, and these discrete wavelength and wave vector values composed the spin-split dispersion.

Theoretical method for dipole emission. To characterize the emission from a single quantum emitter, a monochromatic (linear or circular) electric dipole **p** is assumed at the origin of the Cartesian coordinate system. The emitted electric field **E(r)** from the dipole can be written as[34,35]

$$\mathbf{E}(\mathbf{r}) \propto \overset{\leftrightarrow}{G}(\mathbf{r})\mathbf{p}. \tag{2}$$

Here, $\mathbf{r} = (x, y, z)$ is an arbitrary observation point, and $\overset{\leftrightarrow}{G}(\mathbf{r})$ is the free-space dyadic Green function, which contains all the information about the field components created by the dipole. The dyadic Green function is expressed as

$$\overset{\leftrightarrow}{G}(\mathbf{r}) = \left(\overset{\leftrightarrow}{U} + \frac{1}{k^2}\nabla\nabla\right)G(r), \tag{3}$$

where $\overset{\leftrightarrow}{U}$ is the unit dyadic and k is the wavenumber of the emitted light. The function $G(r) = \exp(ikr)/r$ is the outgoing scalar free-space Green function,

which satisfies the inhomogeneous Helmholtz equation, with a δ-function source term at the origin. Upon performing the derivations, $G(\mathbf{r})$ can also be written in the form

$$\overset{\leftrightarrow}{G}(\mathbf{r}) = \left[\left(\frac{1}{r} + \frac{i}{kr^2} - \frac{1}{k^2r^3}\right)\overset{\leftrightarrow}{U} + \left(-\frac{1}{r} - \frac{3i}{kr^2} + \frac{3}{k^2r^3}\right)\hat{\mathbf{r}}\hat{\mathbf{r}}\right]\exp(ikr), \tag{4}$$

where $\hat{\mathbf{r}}$ is the unit vector in the **r** direction. Consequently, the electric field emitted from the dipole at any observation point can be obtained. To calculate the interaction between the dipole emitter and defect lattice, the dipole emitter is placed at the plane of $z = 0$, and the nanostructures are located at the plane of $z = 0.1\lambda/n_{eff}$.

Numerical simulation. The simulations were implemented using a commercial finite-difference time-domain (FDTD) solver (Lumerical FDTD Solutions). To calculate the defect band for the Berry-phase defective PhC (green dots in Fig. 2a), the Bloch boundaries were employed in the x and y directions, and the antisymmetric boundaries were employed in the z direction. The unit cell of the simulation structure contained six space-variant nanoantennas, which were embedded in the square PhC slab composed of isotropic nanopillars. The structural parameters of the silicon nanostructures (refractive index of 3.4) were set according to the description in Fig. 1c, and the surrounding environment was assumed to be air. Here, due to the negligible material loss and dispersion within the near-infrared PL wavelengths (700–800 nm)[36,37], the refractive index of silicon was assumed to be a single real value. The defects were removed when calculating the band structure for the square PhC slab, and only the primitive cell was simulated. These bands were calculated by employing multiple broadband linear dipole emitters with random locations, orientations and phases, which enabled the excitation of all the resonant modes supported by the structures. To obtain the field distributions for the isolated nanoantenna, PhC slab and Berry-phase defective PhC (Fig. 2d), a monochromatic linear dipole emitter was employed to excite these structures, at the wavelength corresponding to the M point of the defect band.

The dispersion relation employed to fit the defect band (Fig. 2b) is derived in the context of a one-dimensional coupled-resonator optical waveguide, which consists of defect resonators embedded in a two-dimensional photonic crystal[28]. These defect resonators are weakly coupled by the evanescent Bloch waves, so that the eigenmode of the system equals the linear combination of resonant modes of individual resonators, analogous to the spirit of the tight-binding method in condensed-matter physics. Provided that only the nearest-neighbour coupling is considered, the derived dispersion relation satisfies $\omega \propto 1 + \kappa\cos(KR)$, which reveals a hopping mechanism behind the defect band. Here, ω denotes the frequency, κ denotes the coupling factor, K denotes the wavenumber of the defect band in the first Brillouin zone and R denotes the distance between neighbouring resonators. Because of the two-dimensional arrangement of the defects in our Berry-phase defective PhC, the defect band is divided into two parts according to the modal propagation directions: the M–X and M–Γ directions (see first Brillouin zone in Fig. 2a). Each part is considered as a one-dimensional case, which is well fitted by the dispersion relation with an appropriate coupling factor and distance between neighbouring defects. These two parameters (coupling factor and distance) individually determine the amplitude and period of the cosine-shaped defect band, respectively. Note that a stronger hopping effect, evaluated by the coupling factor, is observed along the M–X direction, due to its shorter distance between neighbouring defects. Furthermore, the hopping strength can be controlled by changing the lattice constant of the square lattice (Supplementary Fig. 3c).

Data availability

The data that support the plots within this paper and other findings of this study are available from the corresponding author upon reasonable request.

References

34. Novotny, L. & Hecht, B. *Principles of Nano-optics* (Cambridge Univ. Press, 2006).
35. Neugebauer, M., Banzer, P. & Nechayev, S. Emission of circularly polarized light by a linear dipole. *Sci. Adv.* **5**, eaav7588 (2019).
36. Arbabi, A., Horie, Y., Bagheri, M. & Faraon, A. Dielectric metasurfaces for complete control of phase and polarization with subwavelength spatial resolution and high transmission. *Nat. Nanotechnol.* **10**, 937–943 (2015).
37. Baranov, D. G. et al. All-dielectric nanophotonics: the quest for better materials and fabrication techniques. *Optica* **4**, 814–825 (2017).

Acknowledgements

Author contributions

All authors contributed substantially to this work.

Competing interests

The authors declare no competing interests.

Additional information

Supplementary information is available for this paper at https://doi.org/10.1038/s41565-020-0758-6.

Correspondence and requests for materials should be addressed to E.H.

Peer review information *Nature Nanotechnology* thanks Alexandr Krasnok and the other, anonymous, reviewer(s) for their contribution to the peer review of this work.

Reprints and permissions information is available at www.nature.com/reprints.